analytical chemistry

Article

Multiplex Nucleic Acid Assay of SARS-CoV-2 via a Lanthanide Nanoparticle-Tagging Strategy

Ziyan Li, Xue Chen, Zili Huang, Jing Zhou, Rui Liu,* and Yi Lv*

Cite This: *Anal. Chem.* 2021, 93, 12714−12722

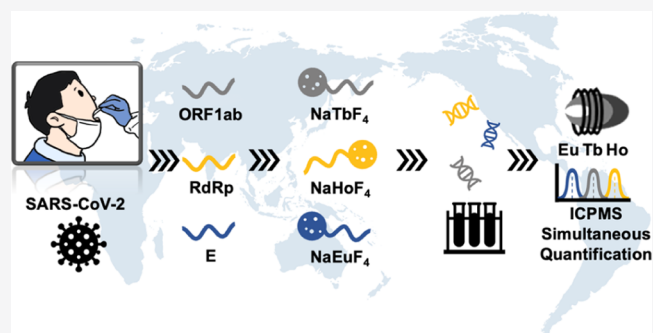Read Online

ACCESS | Metrics & More | Article Recommendations | Supporting Information

ABSTRACT: Early diagnosis, early isolation, and early treatment are efficient solutions to control the COVID-19 pandemic. To achieve the accurate early diagnosis of SARS-CoV-2, a multiplex detection strategy is required for the cross-validation to solve the problem of "false negative" of the existing gold standard assay. Here, we present a multicomponent nucleic acid assay platform for SARS-CoV-2 detection based on lanthanide nanoparticle (LnNP)-tagging strategy. For targeting SARS-CoV-2's RNA fragments ORF1ab gene, RdRp gene, and E gene, three LnNP probes can be used simultaneously to identify three sites in one sample through elemental mass spectrometry detection with limits of detection of 1.2, 1.3, and 1.3 fmol, respectively. With the multisite cross-validation, we envision that this multiplex and sensitive detection platform may provide an effective strategy for SARS-CoV-2 fast screening with a high accuracy.

The pandemic of novel coronavirus disease (COVID-19)[1] by severe acute respiratory syndrome coronavirus 2 (SARS-CoV-2) has led to a surge of a series of serious public health, medical, and society issues. Early diagnosis, early isolation, and early treatment are efficient solutions to control the COVID-19 pandemic. As one of the diagnostic criteria, computerized tomography images can only provide a diagnosis accuracy of 76.4%.[2] Antibody-based serological tests are not suitable for the early diagnosis[3,4] because they are not produced until 3 weeks after infection.[5] The two currently used nucleic acid pathogenic diagnoses are nucleic acid sequencing and nucleic acid fluorescence quantitative polymerase chain reaction (qPCR).[6] Nucleic acid sequencing is relatively time-consuming and expensive.[7] As the current gold standard, qPCR falls in a dilemma of "false negative".[8,9] Up to 20 to 67% of patients are tested positive only after multiple repeated tests,[10] as also described in National Health Commission of China's new coronavirus pneumonia diagnosis and treatment plan.[11]

To achieve the accurate diagnosis of SARS-CoV-2, a multiplexed detection strategy is required for multiple characteristic-related markers for the cross-validation. The U.S. Centers for Disease Control (CDC) gives examples of recommended gene selection and multicomponent testing methods.[12] World Health Organization (WHO) recommends three qPCR reactions to confirm COVID-19 infection, while a total of 3 qPCR tests were performed sequentially for each patient sample.[13] Besides, electrochemical biosensors,[14] colorimetric sensors,[15] a loop-mediated isothermal amplification (LAMP) combined with clustered regularly interspaced

short palindromic repeats (CRISPER) system,[16,17] microfluidic assay,[6] and point-of-care testing (POCT) platforms[18] have been developed for single or multicomponent detection.[19−23] Despite great success,[24] these optical and electrochemical strategies are practically limited by spectral overlap-caused interference for the simultaneous multicomponent detection.[25]

Elemental mass spectrometry, especially inductively coupled plasma mass spectrometry (ICPMS),[26−28] is emerging as a powerful platform for the multiplex bioassay[29−31] due to its high sensitivity,[32] wide dynamic range,[33] and multiplex sensing ability.[34−36] The multiplex bioassay by ICPMS[37] possesses many superiorities, such as a low sample consumption,[38] a short analysis time, a simplified procedure, and a low cost.[38−40] Zhang's group developed a multiplex nucleic acid assay and immunoassay by lanthanide macrocyclic compound tagging.[41,42] Wang et al. performed a multiplex assay for protease markers.[43] Simultaneous detection of multiple microRNAs by the MNAzyme-catalyzed amplification assay was realized,[44] while single-particle mode ICPMS was applied for a three-component homogeneous immunoassay of pancreatic cancer.[45] Multicomponent marker and disease subtype analysis provides the possibility of the cross-validation through a
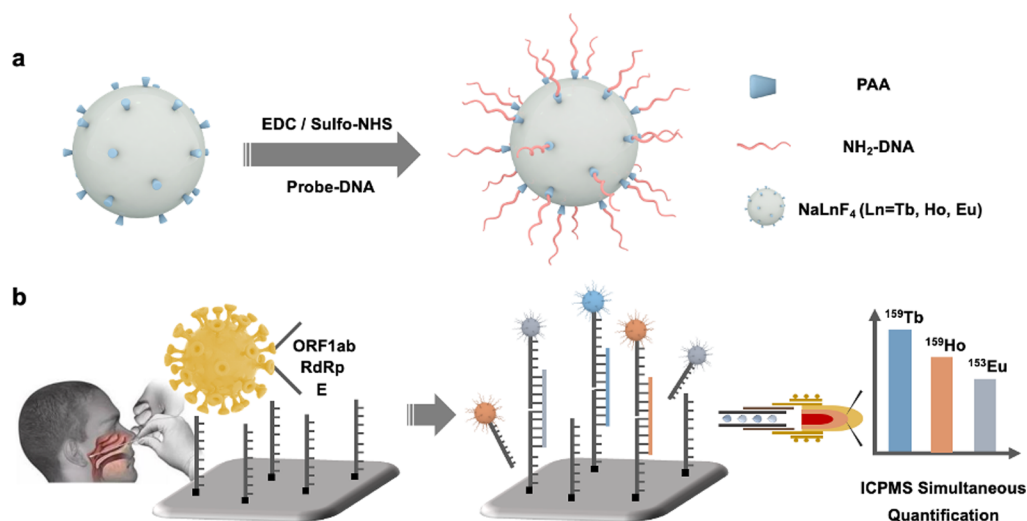
Figure 1. (a) Schematic illustration of the functionalization of $NaLnF_4$ NPs (Ln = Tb, Ho, and Eu). PAA-coated NPs were obtained by one-pot solvent thermal preparation to facilitate further conjugation with NH_2-functionalized capture DNA to form a capture probe. (b) Schematic illustration of the multiplexed assay process. RNA fragments ORF1ab, RdRp, and E were anchored on the MBs by interacting with capture DNA attached to MBs and labeled with $NaLnF_4$ NP-probe DNA, which allows the ultrasensitive ICPMS detection of the dissolute Ln^{3+}-chelates.

simultaneous monitoring of multiple parameters,[46] which plays a significant role in improving the accuracy of the disease diagnosis. However, the existing assay formats are not compatible with the direct detection of SARS-CoV-2, which is mainly limited by the low sensitivity of macrocyclic compound element labels.

Herein, we proposed a multiplexed nucleic acid assay for improving the detection rate of SARS-CoV-2 via lanthanide nanoparticle (NP)-tagging strategy. Three lanthanide NP (LnNPs, Ln = Tb, Ho, and Eu)-based nanoprobes were designed and applied to detect SARS-CoV-2's ORF1ab gene, RdRp gene, and E gene. Three kinds of capture DNA attached to magnetic beads (MBs) could hybridize with corresponding targets, and the half remaining chain could also hybridize with the as-prepared probe DNA-modified NPs. LnNP tags were digested in the enhancer solution and released lanthanide ions from NPs to those of the β-NTA-$Tb^{3+}/Ho^{3+}/Eu^{3+}$−TOPO complex.[47] The LnNPs are ideal multiplex labels[48] because lanthanides are numerous and similar in nature,[49] and there are 55 to 64 atoms exist per nm^{-3} NP.[50] Thanks to multiatoms inside each NP, a high sensitivity is obtained without the need of complex nucleic acid amplification procedures.

■ EXPERIMENTAL SECTION

Apparatus and Reagents. A PerkinElmer NexION 350 inductively coupled plasma mass spectrometer was used to detect ^{153}Eu, ^{159}Tb, and ^{165}Ho in standard mode. The operating conditions are listed in Table S1. Apparatus for characterization and detection is provided in the Supporting Information. Other details about reagents and materials used are also provided in it. DNA and RNA sequences used in this work are also listed in Table S2, Supporting Information.

Synthesis of −COOH-Functionalized $NaLnF_4$ (Ln = ^{153}Eu, ^{159}Tb, and ^{165}Ho) NPs. Carboxylic acid-functionalized $NaLnF_4$ (Ln = ^{153}Eu, ^{159}Tb, and ^{165}Ho) NPs were synthesized as bioprobes adopting a one-step solvothermal route by employing polyacrylic acid (PAA) as the surfactant and a capping ligand, both of which provide excess −COOH for further bioconjugation and improving NPs' hydrophilicity (Figure 1a). Details are given in the Supporting Information.

Preparation of Probe DNA-$NaLnF_4$ NPs (O/R/E-Tb/Ho/Eu NPs). To prepare probe DNA-$NaLnF_4$ NPs as a signal reporter, NH_2-modified probe DNA was directly attached with the −COOH group coating on the $NaLnF_4$ surface through the EDC−NHS (N-ethyl-N′-(3-(dimethyl-amino)propyl)-carbodiimide-N-hydroxy succinimide)reaction. Specific details of the labeling process are given in the Supporting Information. After ligation, NPs were blocked with 2% bovine serum albumin (BSA) in TBS buffer to prevent protein's nonspecific binding and the residue carboxylic acid groups were blocked with excess tris in TBS buffer. Subsequently, the as-prepared probe DNA-$NaLnF_4$ NPs were diluted to 1.8 mL per OD DNA and made ready to use.

Preparation of Capture DNA-MBs (Capture O/R/E-MB). The process of attaching oligonucleotides on MBs was carried out according to the instructions of Dynabeads M-280. Ahead of all, pretreatment to avoid RNase contamination for RNA manipulation was performed, then biotinylated capture DNA was immobilized, specific details are given in Supporting Information. Following that the MBs with 2% BSA were blocked to prevent nonspecific binding, and the DNA-coated MBs were redispersed in 100 μL Tris-HCl buffer stored at 4 °C for further use.

Analysis of ORF1ab by Sandwich Assay-ICPMS. Before multicomponent RNA fragment detection, the feasibility and conditions of a single component assay were surveyed by utilizing ORF1ab as a model SARS-CoV-2 positive gene. To fulfill it, a certain amount of capture O-MBs was used for each sample with blocking ahead, 0 and 2 pmol ORF1ab were added under different conditions. Subsequently, probe O-$NaTbF_4$ NPs participate and react for fully chain hybridization. After the reaction is completed, 200 μL enhancer solution was utilized to release ions from the formed structure for ICPMS quantification.

Simultaneous Analysis of ORF1ab/RdRp/E by Sandwich Assay-ICPMS. The RNA sandwich hybridization system was 7.5 μL capture DNA-MBs. Because of the specific recognition between capture O/R/E-MB, targets O/R/E, and probe DNA-$NaLnF_4$ NPs (O/R/E-Tb/Ho/Eu NPs), a sandwich-like structure was formed with MBs as both solid-
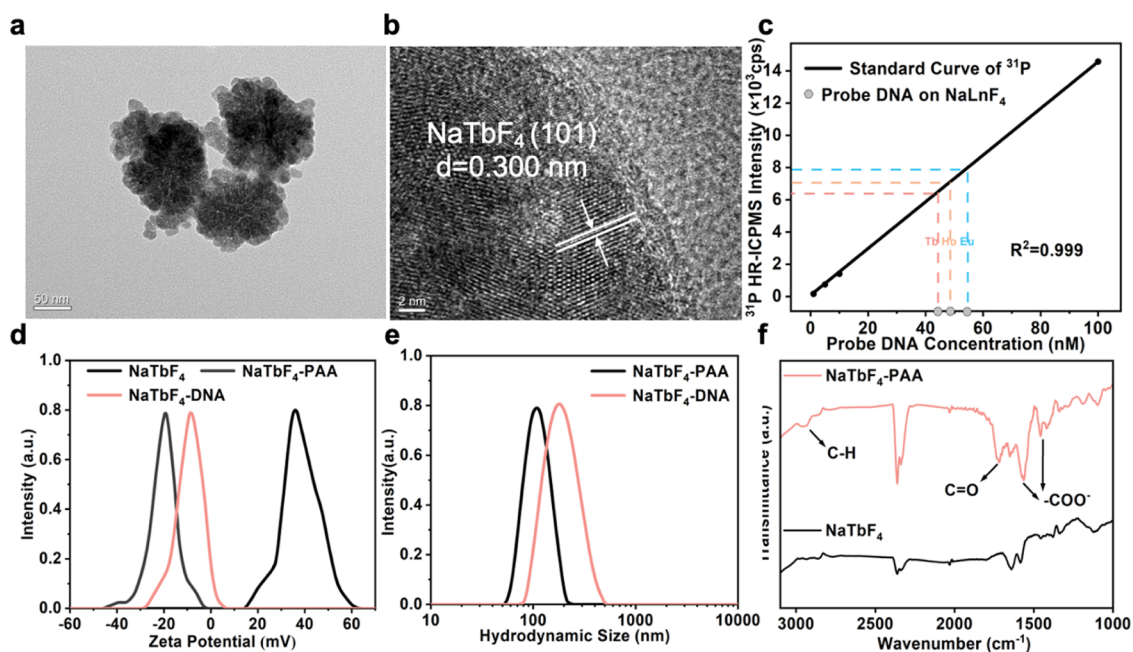
Figure 2. (a) TEM image of the as-prepared $NaTbF_4$–PAA. (b) HR-TEM image of $NaTbF_4$–PAA. (c) Quantification of probe DNA concentration with inner label ^{31}P in each sample detected by HR-ICPMS. (d) Zeta potential of naked $NaTbF_4$, $NaTbF_4$–PAA, and $NaTbF_4$-DNA. (e) Particle size distribution of naked $NaTbF_4$, $NaTbF_4$–PAA, and $NaTbF_4$-DNA. (f) FTIR spectra of the naked $NaTbF_4$ and $NaTbF_4$–PAA. Feature peaks of the functional groups are marked.
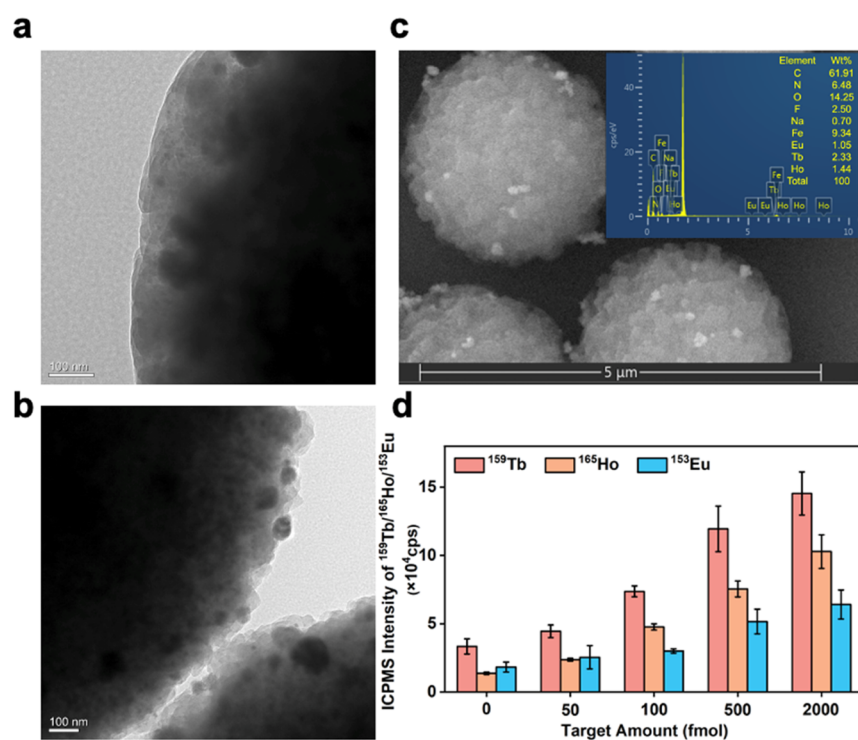

Figure 3. TEM of (a) naked MBs, (b) as-synthesized $NaTbF_4$, $NaHoF_4$, and $NaEuF_4$ NPs attached on MBs after hybridization. (c) SEM and EDS spectrum of the as-synthesized $NaTbF_4$, $NaHoF_4$, and $NaEuF_4$ NPs attached on MBs after hybridization. (d) Multiplex RNA fragment assay based on ICPMS. ORF1ab, RdRp, and E were simultaneously analyzed with different concentrations (0, 50, 100, 500, and 2000 fmol).

phase reaction matrix and separation platform. Release of $Tb^{3+}/Ho^{3+}/Eu^{3+}$ from the NPs and the formation of the β-NTA-$Tb^{3+}/Ho^{3+}/Eu^{3+}$–TOPO complex enhancer solution and the digested solution were diluted and send to the ICPMS for final $^{153}Eu/^{159}Tb/^{165}Ho$ quantification (Figure 1b). Because ICPMS exhibits accurate quantitative capacity and a

wide detection range (Figure S1) for the three lanthanides we adopted, we can convert the amount of target according to signal strength.

Preparation of Viral RNA Extraction for Standard Recovery Experiment. The real sample matrix of three throat swab samples for the recovery experiment was collected
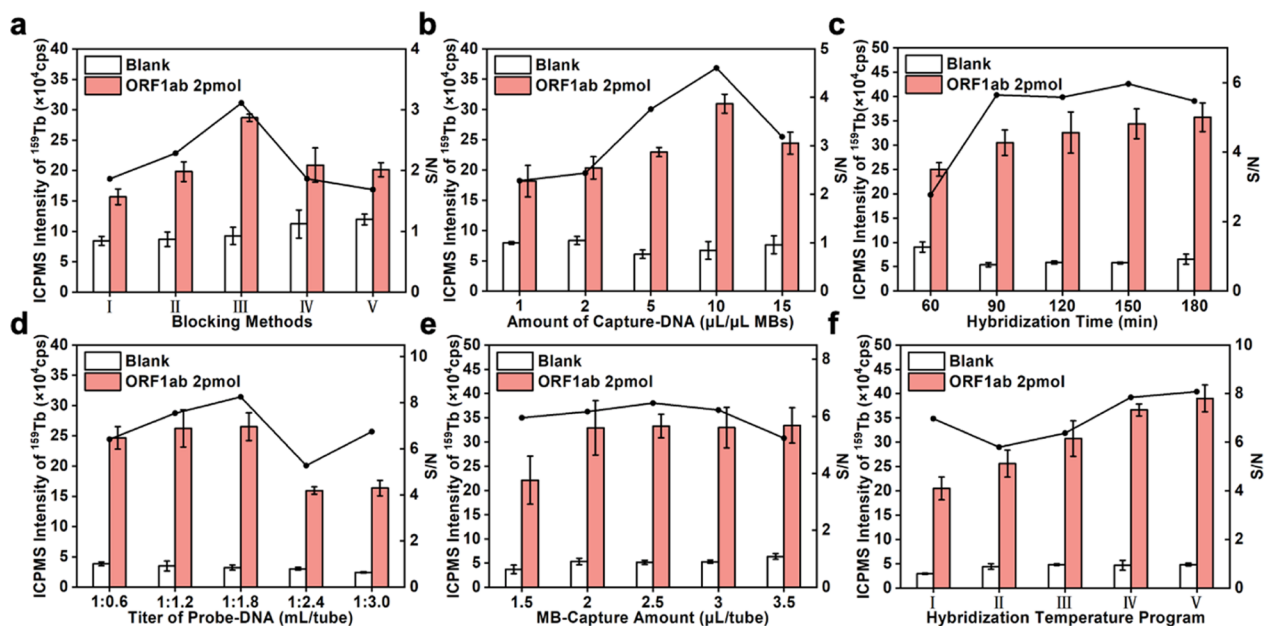
Figure 4. Optimization of reaction conditions (a) effects of different blocking methods: (I) 2% BSA, overnight. (II) 2% BSA, 1 h. (III) 2% BSA, 30 min. (IV) 2% BSA, wash. (V) 2% skim milk, 30 min. (b) Effects of the amount of capture-DNA added to MBs on the ICPMS intensity. (c) Effects of hybridization time on the ICPMS intensity. (d) Effects of titer for as-prepared probe-DNA, per tube, containing 60 μL nanoparticles and 1OD DNA to a final volume of 1 mL and then diluted. (e) Effects of the as-prepared MB-capture amount per tube of a sample. (f) Effect of the hybridization temperature program: (I) 25 °C, 150 min. (II) 37 °C, 150 min. (III) 43 °C, 90 min, then 25 °C, 60 min. (IV) 43 °C, 120 min then 25 °C, 30 min. (V) 43 °C, 150 min.

using the RNA viral sample collection tubes and purified using the EZ-10 spin column viral total RNA extraction kit. Specific experimental steps are given in Supporting Information.

■ RESULTS AND DISCUSSION

Characterization of PAA−NaLnF$_4$, Probe DNA-NaLnF$_4$ NPs, and the Capture DNA-MBs. *Characterization of PAA−NaLnF$_4$.* Transmission electron microscopy (TEM) shows the spherical morphology of the NaTbF$_4$ particles at about 100 nm (Figure 2a). It is worth noting that in these TEM figures, we can see the edges of the NPs have a slightly bright thin layer, which proves that the surface of the NPs is coated with PAA. The high-resolution TEM image (Figure 2b) shows lattice fringes with an observed *d*-spacing of 0.300 nm, which is in good agreement with the lattice spacing in the (101) planes of hexagonal NaTbF$_4$ (PDF #27-0809). The X-ray powder diffraction (XRD) patterns of the NPs exhibit peak position and intensities that can be well indexed in accord with NaTbF$_4$ crystals (Figure S2a). Elements and corresponding proportions of a kind of particles by X-ray photoelectron spectroscopy (XPS) analysis give a peak area of Na, Tb, and F about 1:1:4 (Figure S3a). The one-step method also wraps the carboxyl group in the surface of the synthesis of the NPs, and the zeta potential of the naked NPs is positive. The NPs wrapped in the PAA encircled by the method exhibit negative electrical properties (Figure 2d). Similarly, in the Fourier transform infrared spectroscopy (FTIR), the PAA-modified NPs exhibit a carboxyl group characteristic peak compared to bare NPs (Figure 2f). Those of the other two NPs were similar, and detailed properties characterized by TEM and high resolution TEM (HRTEM) (Figures S4, S5), XRD and XPS (Figures S2, S3), zeta potential (Figure S6), and IR (Figure S8) are given in Supporting Information.
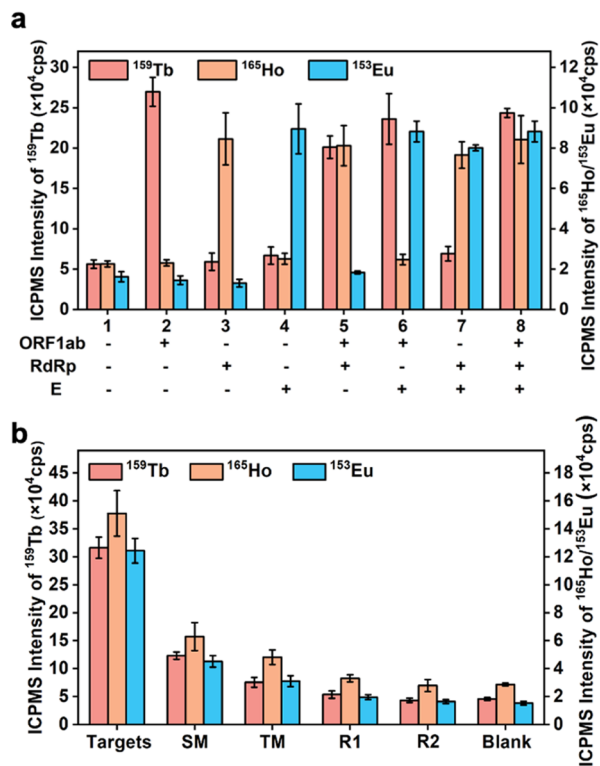

Figure 5. (a) Selectivity and cross-reactivity of the developed ICPMS-based multiple RNA fragment assay. (1) Blank, (2) ORF1ab, (3) RdRp, (4) E, (5) ORF1ab + RdRp, (6) ORF1ab + E, (7) RdRp + ORF1ab, and (8) ORF1ab + RdRp + E. (b) Specificity of this method for the homologous sequences of ORF1ab, RdRp, and E. "SM": single-mismatched targets and "TM": triple-mismatched targets.

Table 1. Analytical Performance of ORF1ab/RdRp/E Based on ICPMS

target RNA	linear range (fmol)	linear relationship	R^2	LOD (fmol)
ORF1ab	20−4000	$y = 112{,}372 \lg x - 11{,}479$	0.991	1.2
RdRp	20−4000	$y = 26{,}165 \lg x - 14{,}056$	0.991	1.3
E	20−4000	$y = 29\,967 \lg x - 24{,}277$	0.990	1.3

Characterization of Probe DNA-NaLnF₄ NPs. Characterization of Probe DNA-NaLnF$_4$ NPs is essential for our increased understanding of bioconjugation. This modification process can be characterized by multiple means. To understand the contents of the DNA attached to the nanoprobe we added for each sample, we used the high-resolution ICPMS (HR-ICPMS) to quantitatively analyze ^{31}P on the nanoprobes.[51] We use the same length of DNA as used for a standard curve of the P element, then make a quantity of probe DNA (Figure 2c), and it is concluded that each sample substantially corresponds to 8 pmol of probe added, with a similar connecting efficiency of each NP. The modification process was also validated by zeta potential with noticeable change (Figure 2d). In addition, dynamic light scattering (DLS) determined the increase of the particle size after DNA ligation. Characterization of the other NPs using zeta potential (Figure S6) and DLS (Figure S7) is given in Supporting Information.

Characterization of Capture DNA-MBs. The capture DNA-MBs were prepared by coupling all three capture DNA with the same molar concentration onto SA-MBs in a one-pot process because it has similar analysis performance compared to separate coupling (Figure S9). In theory, each type of capture DNA strand accounted for one-third of the total attached capture DNA. Changes in zeta-potential (Figure S10a) and hydrodynamic size (Figure S10b) revealed

Table 2. Results of Standard Recovery Experiment in Virus RNA Extract

sample	target RNA	added (fmol)	found (fmol)	recovery (%)
1#	ORF1ab	0	not found	
		200	181 ± 11.6	90
		2000	1848 ± 177	92
	RdRp	0	not found	
		200	189 ± 25.8	94
		2000	2041 ± 211	102
	E	0	not found	
		200	183 ± 12.9	92
		2000	2083 ± 121	104
2#	ORF1ab	0	not found	
		200	190 ± 11.4	95
		2000	1934 ± 105	97
	RdRp	0	not found	
		200	213 ± 43.4	106
		2000	1928 ± 118	96
	E	0	not found	
		200	191 ± 10.7	96
		2000	1958 ± 49.0	98
3#	ORF1ab	0	not found	
		200	224 ± 17.9	112
		2000	1855 ± 68.4	93
	RdRp	0	not found	
		200	196 ± 32.6	98
		2000	1810 ± 143	91
	E	0	not found	
		200	208 ± 8.80	104
		2000	1870 ± 129	94

successful coupling outcomes. Our values also match the instructions of Dynabeads M280.
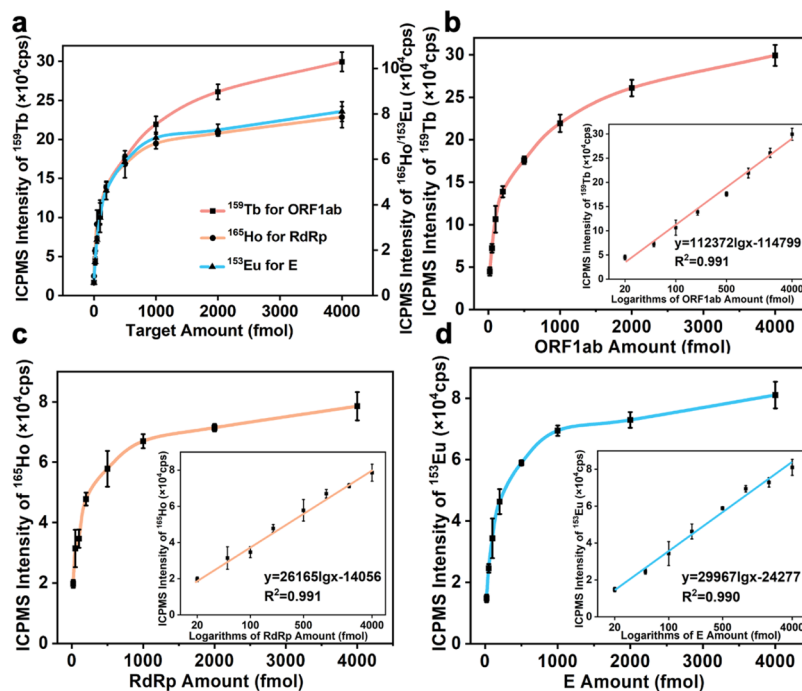

Figure 6. (a) Simultaneous detection of ORF1ab/RdRp/E and relationship between the signal intensities of ^{159}Tb/^{165}Ho/^{153}Eu and the concentrations of ORF1ab/RdRp/E. Linear range with the inset graph showing the calibration curves of (a) ORF1ab, (b) RdRp, and (c) E based on ICP−MS.

Table 3. Summary of Three Detection Approaches Used in Detecting SARS-CoV-2 Nucleic Acid and Two Multiplexed Nucleic Acid Assay by ICPMS

techniques	advantages	limitations	linear range	LOD	refs
RT-qPCR	multiplexed Assay	spectral overlap		2 copies/μL	23
electrochemical sensors	rapid detection	unable multiplexed assay		26 fM	14
POCT	ultrafast and recyclable	unable multiplexed assay		0.843 nM	18
element tagging ICPMS assay	multiplexed Assay	narrow detection range	0.84−20 pmol	0.84 pmol	41
DSN amplification ICPMS assay	multiplexed Assay	low sensitivity	58−200 fmol	48 fmol	48

Feasibility of the Sandwich Assay-ICPMS Strategy. To test the feasibility of the developed multiplex SARS-CoV-2 RNA fragment assay, ICPMS detection under different conditions was done (Figure S11). Another more intuitive evidence is that under TEM, it shows naked MBs without immobilization in Figure 3a. After hybridization, three kinds of NPs were attached. Several NaTbF$_4$, NaHoF$_4$, and NaEuF$_4$ could be observed clearly (Figure 3b). A similar phenomenon could also be observed in the SEM image (Figure S12) with its inset graph giving the compositional analysis by energy-dispersive X-ray spectroscopy (EDS). There emerged elemental peaks of Tb, Ho, and Eu in the EDS diagram, and small particles could be found on MBs (Figure 3c). The above evidence demonstrated successful hybridization, and a sandwich structure was formed. To further prove this strategy's feasibility, five artificial samples containing different concentrations of ORF1ab, RdRp, and E were prepared and hybridized with capture O/R/E-MBs and O/R/E-Tb/Ho/Eu NPs. With the increase in ORF1ab, RdRp, and E concentrations, the signal intensities of ^{159}Tb, ^{165}Ho, and ^{153}Eu also increased (Figure 3d).

Optimization of Experimental Conditions. Experimentally, one of the RNA fragments, ORF1ab with the corresponding tagging NP NaTbF$_4$, was chosen as the model RNA for optimizing experimental conditions. It has a similar length to the other two components of the test object, so the corresponding characteristics such as Tm are similar. Based on this, various experimental parameters were optimized using blocking methods, reaction time and temperature, and the number of components of this system (capture DNA, capture-MB, and probe-DNA). The specific details about the reaction are given in Supporting Information.

Effects of Different Blocking Methods. NPs will have nonspecific adsorption of some molecules due to their nanoscale effects. We use proteins to block the remaining sites of the NPs that have been bound to DNA that may be nonspecifically adsorbed. Figure 4a reveals that there has been a steep decline in the signal when the blocking condition is not suitable for this system. The blocking condition we finally selected is 2% BSA, 30 min.

Effects of the Amount of Capture-DNA Added to MBs. In a further set of experiments, we explored the reaction ratio of MBs to captured DNA (Figure 4b). According to the binding capacity instructions of the MBs, we have selected a range of DNA concentrations to achieve the maximum binding efficiency and at the same time to ensure that DNA addition is not too excessive to cause insufficient washing in which free DNA might lead to interference on subsequent sandwich hybridization reactions. Finally, the condition we selected is the group with the highest signal-to-noise ratio, that is, when the concentration of capture DNA is 2 μM, the volume ratio of DNA to MBs is 10:1.

Effects of Hybridization Time. Hybridization time is a common condition that has a considerable impact on reaction efficiency. To guarantee enough time and control nonspecific adsorption, we explored the reaction efficiency in the time range of 60−180 min, as shown in Figure 4c. Taking signal growth and blank control as dual considerations, as time grows, the signal value first shows an upward trend and then gradually stabilizes, while the blank value first decreases due to the competition of the target molecule and then increases due to time. Considering the signal-to-noise ratio, we choose 150 min as the best hybridization time.

Effects of the Titer for As-prepared Probe-DNA. What can be seen in Figure 4d is the influence of probes of different titers on the experimental results. For 60 μL NPs and 1OD DNA per tube; the corresponding condition is the diluted volume of each probe, ranging from 0.6 to 3.0 mL. From the changing trend of the signal and blank value in the figure, when the probe is more concentrated and the titer is relatively low, the NPs on the excess probe will produce more nonspecific adsorption on the reaction substrate. As the temperature increases, the blank gradually decreases, but if the probe is too dilute, the concentration of probe DNA used to bind the target will decrease, and the reaction speed and efficiency will subside, too, making it impossible to obtain high signal values. Taking these effects into consideration, we assumed that the titer 1 to 1.8 mL with the highest signal-to-noise ratio was selected for applying under subsequent experimental conditions.

Effects of the As-prepared MB-Capture Amount. As the unit of the sandwich structure, MB-capture and Probe-DNA have similar influence trends on the reaction. Under the premise of ensuring the amount for reaction, as a reaction matrix, the increase of MBs is positively correlated with the increase in nonspecific adsorption (Figure 4e). Therefore, we choose a moderate amount, 2.5 μL per sample, and perform subsequent reactions under this condition.

Effect of the Hybridization Temperature Program. We studied the appropriate time for the interaction. Under the same reaction time, when the selected reaction temperature is below the melting temperature (T_m) of 15−20 °C of the target sequence, the reaction would be more efficient; the lower the temperature, the more stable the double-stranded binding DNA. To explore the checks and balances of these two factors, we have designed a series of hybridization temperature programs as shown in Figure 4f. When the temperature is 43 °C, the best signal-to-noise ratio can be obtained. Finally, 43 °C was chosen as the optimum reaction temperature.

Specificity and Selectivity. When multiple components are the target to be analyzed, it is necessary to ensure that there will be no mutual influence between them. We experimentally prove the mechanism of this strategy and demonstrate its specificity. We have prepared a series of target gene fragment solutions with different components, as shown in Figure 5a.

According to the signal intensity of lanthanide metal ions corresponding to different target combinations in the histogram, we can see those signals of ^{159}Tb/^{165}Ho/^{153}Eu upon the addition of corresponding RNAs were much higher than their blank signals; whether it is a single component or a mixture of any two components, even the three components are tested together, it shows independent and steady results demonstrating reasonable specificity of the method.

Similarly, there may be a variety of nontarget nucleic acid fragments in real samples. Due to the high sequence homology of RNA, we detected a series of sequences similar to the three targets to prove the selectivity of the established strategy. The results are shown in Figure 5b. Experimental groups were containing single-mismatched RNA fragments and triple-mismatched RNA fragments of both ORF1ab/RdRp/E. What is more, random RNA and random DNA were also detected, and the results were similar to those of blank groups, indicating a decent selectivity.

Analytical Performance. After optimizing a series of reaction conditions, we explored the analytical performance of the established analytical method as listed in Table 1. In the simultaneous detection strategy, the calibration curves were built up with varieties of RNA fragment (ORF1ab, RdRp, and E) concentrations (0, 20, 50, 100, 200, 500, 1000, 2000, and 4000) and ICPMS signal intensities of lanthanide elements (^{159}Tb/^{165}Ho/^{153}Eu). As shown in Figure 6a, the three targets can be mixed and quantified and have similar growth trends. In the inset figures of Figure 6b–d, after we perform logarithmic processing and linear fitting of the data, decent linear relationships were obtained at 20–4000 fmol for ORF1ab, RdRp, and E with equations $y = 112{,}372 \lg x - 11{,}479$, $y = 112{,}372 \lg x - 11{,}479$, and $y = 29{,}967 \lg x - 24{,}277$. The limits of detection ($3\sigma/k$, LODs) for ORF1ab, RdRp, and E were 1.2, 1.3, and 1.3 fmol, respectively.

For investigating the self-magnification of this strategy, the analytical performance was compared with those of other multicomponent simultaneous analysis methods by ICPMS. We use lanthanide NPs as element markers. Compared with the traditional macrocyclic compound-lanthanide element tagging, it has a more comprehensive linear range and three orders of magnitude higher sensitivity; compared with the DSN amplification strategy, the LOD was decreased by 40-fold (Table 3). This shows that even working with the simplest sandwich hybrid structure, our strategy can achieve higher sensitivity and high multiplicity without additional amplification reactions.

Recoveries and Determined Results. Healthy human throat swab samples were collected, purified, collected, spiked, and analyzed to evaluate the method's applicability. To investigate the influence of the matrix, three target RNAs numbered as 1#, 2#, and 3# were spiked in RNA extraction solution simultaneously at the concentrations of 0, 200, and 2000 fmol. Moreover, the spiked samples were subjected to the proposed method. Quantitative recovery outcomes are all listed in Table 2. As shown, 181 fmol of ORF1ab, 189 fmol of RdRp, and 183 fmol of E were simultaneously found. The recoveries of 90, 94, and 92% were gained when 200 fmol RNA was added and extracted in the 1# throat swab sample. The spiked recovery results of other matrix samples at different concentrations are also within the range of 90−112%. Thus, it has added robust evidence for tolerance of the RNA virus extraction sample matrix and showed prospects of this strategy for the actual application of the experiments.

CONCLUSIONS

In this work, we have established a multiplexed sandwich RNA analytical method based on NP self-enhanced RNA analysis to detect three specific RNA gene sites of SARS-CoV-2 simultaneously. Three lanthanide NP probes synthesized by the one-step solvent thermal method are modified by a carboxyl group and further coupled with DNA to perform signal report units. Meanwhile, with the chelating ability of β-NTA and the magnetic properties of SA-MBs, the lanthanide tag as the multiplexed probe can be quickly released in the form of ions to form a uniform solution. Thus, high-sensitivity detection can be realized through the self-amplification of NPs. If other nucleic acid amplification strategies are introduced into the system, the sensitivity can be further improved. We expect that this detection platform can increase the detection rate of SARS-CoV-2 through the simultaneous detection of multiple genes, and this strategy can be extended to the sensitive simultaneous detection of other nucleic acids or biomarkers.

ASSOCIATED CONTENT

Supporting Information

The Supporting Information is available free of charge at https://pubs.acs.org/doi/10.1021/acs.analchem.1c02657.

> Experimental details including the apparatus, materials, and reagents used; synthesis of NPs; preparation of probes; recovery RNA samples; characterization of NPs using XPS, XRD, SEM, TEM and HRTEM, FTIR, and size and zeta potential of the probe; operating parameters of ICP−MS and DNA sequences (PDF)

AUTHOR INFORMATION

Corresponding Authors

Rui Liu − *Key Laboratory of Green Chemistry & Technology, Ministry of Education, College of Chemistry, Sichuan University, Chengdu 610064 Sichuan, China;* ⊙ orcid.org/0000-0001-9928-5373; Phone: +86-28-8541-2398; Email: liur@scu.edu.cn; Fax: +86-28-8541-2398

Yi Lv − *Analytical & Testing Center, Sichuan University, Chengdu 610064 Sichuan, China;* ⊙ orcid.org/0000-0002-7104-2414; Email: lvy@scu.edu.cn

Authors

Ziyan Li − *Analytical & Testing Center, Sichuan University, Chengdu 610064 Sichuan, China*

Xue Chen − *Key Laboratory of Green Chemistry & Technology, Ministry of Education, College of Chemistry, Sichuan University, Chengdu 610064 Sichuan, China*

Zili Huang − *Key Laboratory of Green Chemistry & Technology, Ministry of Education, College of Chemistry, Sichuan University, Chengdu 610064 Sichuan, China*

Jing Zhou − *Analytical & Testing Center, Sichuan University, Chengdu 610064 Sichuan, China*

Complete contact information is available at:
https://pubs.acs.org/10.1021/acs.analchem.1c02657

Notes

The authors declare no competing financial interest.

■ REFERENCES

(1) Zhu, N.; Zhang, D.; Wang, W.; Li, X.; Yang, B.; Song, J.; Zhao, X.; Huang, B.; Shi, W.; Lu, R.; Niu, P.; Zhan, F.; Ma, X.; Wang, D.; Xu, W.; Wu, G.; Gao, G. F.; Tan, W.; China Novel Coronavirus, I.; Research, T. *N. Engl. J. Med.* **2020**, *382*, 727−733.

(2) Guan, W.-j.; Ni, Z.-y.; Hu, Y.; Liang, W.-h.; Ou, C.-q.; He, J.-x.; Liu, L.; Shan, H.; Lei, C.-l.; Hui, D. S. C.; Du, B.; Li, L.-j.; Zeng, G.; Yuen, K.-Y.; Chen, R.-c.; Tang, C.-l.; Wang, T.; Chen, P.-y.; Xiang, J.; Li, S.-y.; Wang, J.-l.; Liang, Z.-j.; Peng, Y.-x.; Wei, L.; Liu, Y.; Hu, Y.-h.; Peng, P.; Wang, J.-m.; Liu, J.-y.; Chen, Z.; Li, G.; Zheng, Z.-j.; Qiu, S.-q.; Luo, J.; Ye, C.-j.; Zhu, S.-y.; Zhong, N.-s. *N. Engl. J. Med.* **2020**, *382*, 1708−1720.

(3) Poh, C. M.; Carissimo, G.; Wang, B.; Amrun, S. N.; Lee, C. Y.-P.; Chee, R. S.-L.; Fong, S.-W.; Yeo, N. K.-W.; Lee, W.-H.; Torres-Ruesta, A.; Leo, Y.-S.; Chen, M. I.-C.; Tan, S.-Y.; Chai, L. Y. A.; Kalimuddin, S.; Kheng, S. S. G.; Thien, S.-Y.; Young, B. E.; Lye, D. C.; Hanson, B. J.; Wang, C.-I.; Renia, L.; Ng, L. F. P. *Nat. Commun.* **2020**, *11*, 2806.

(4) Ng, D. L.; Goldgof, G. M.; Shy, B. R.; Levine, A. G.; Balcerek, J.; Bapat, S. P.; Prostko, J.; Rodgers, M.; Coller, K.; Pearce, S.; Franz, S.; Du, L.; Stone, M.; Pillai, S. K.; Sotomayor-Gonzalez, A.; Servellita, V.; Martin, C. S. S.; Granados, A.; Glasner, D. R.; Han, L. M.; Truong, K.; Akagi, N.; Nguyen, D. N.; Neumann, N. M.; Qazi, D.; Hsu, E.; Gu, W.; Santos, Y. A.; Custer, B.; Green, V.; Williamson, P.; Hills, N. K.; Lu, C. M.; Whitman, J. D.; Stramer, S. L.; Wang, C.; Reyes, K.; Hakim, J. M. C.; Sujishi, K.; Alazzeh, F.; Pham, L.; Thornborrow, E.; Oon, C.-Y.; Miller, S.; Kurtz, T.; Simmons, G.; Hackett, J., Jr.; Busch, M. P.; Chiu, C. Y. *Nat. Commun.* **2020**, *11*, 4698.

(5) Zhao, J.; Yuan, Q.; Wang, H.; Liu, W.; Liao, X.; Su, Y.; Wang, X.; Yuan, J.; Li, T.; Li, J.; Qian, S.; Hong, C.; Wang, F.; Liu, Y.; Wang, Z.; He, Q.; Li, Z.; He, B.; Zhang, T.; Fu, Y.; Ge, S.; Liu, L.; Zhang, J.; Xia, N.; Zhang, Z. *Clin. Infect. Dis.* **2020**, *71*, 2027−2034.

(6) Xiong, H.; Ye, X.; Li, Y.; Wang, L.; Zhang, J.; Fang, X.; Kong, J. *Anal. Chem.* **2020**, *92*, 14297−14302.

(7) Smyrlaki, I.; Ekman, M.; Lentini, A.; Rufino de Sousa, N.; Papanicolaou, N.; Vondracek, M.; Aarum, J.; Safari, H.; Muradrasoli, S.; Rothfuchs, A. G.; Albert, J.; Högberg, B.; Reinius, B. *Nat. Commun.* **2020**, *11*, 4812.

(8) West, C. P.; Montori, V. M.; Sampathkumar, P. *Mayo Clin. Proc.* **2020**, *95*, 1127−1129.

(9) Kinloch, N. N.; Ritchie, G.; Brumme, C. J.; Dong, W.; Dong, W.; Lawson, T.; Jones, R. B.; Montaner, J. S. G.; Leung, V.; Romney, M. G.; Stefanovic, A.; Matic, N.; Lowe, C. F.; Brumme, Z. L. *J. Infect. Dis.* **2020**, *222*, 899−902.

(10) Wiersinga, W. J.; Rhodes, A.; Cheng, A. C.; Peacock, S. J.; Prescott, H. C. *JAMA* **2020**, *324*, 782−793.

(11) National Health Commission of the People's Republic of China and Traditional Chinese Medicine of the People's Republic of China (2020) Guidelines for the Diagnosis and Treatment of Coronavirus Disease 2019 (Trial Version 7).

(12) CDC. *CDC 2019-Novel Coronavirus (2019-nCoV) Real-Time RT-PCR Diagnostic Panel SOP# CDC-006-00019*, 2020.

(13) CDC. *CDC 2019-nCoV Real-Time RT-PCR Diagnostic Panel Product Information Sheet SOP# CDC-006-00006*, 2020.

(14) Peng, Y.; Pan, Y.; Sun, Z.; Li, J.; Yi, Y.; Yang, J.; Li, G. *Biosens. Bioelectron.* **2021**, *186*, 113309.

(15) Karami, A.; Hasani, M.; Azizi Jalilian, F.; Ezati, R. *Sens. Actuators B Chem.* **2021**, *328*, 128971.

(16) Arizti-Sanz, J.; Freije, C. A.; Stanton, A. C.; Petros, B. A.; Boehm, C. K.; Siddiqui, S.; Shaw, B. M.; Adams, G.; Kosoko-Thoroddsen, T.-S. F.; Kemball, M. E.; Uwanibe, J. N.; Ajogbasile, F.

V.; Eromon, P. E.; Gross, R.; Wronka, L.; Caviness, K.; Hensley, L. E.; Bergman, N. H.; MacInnis, B. L.; Happi, C. T.; Lemieux, J. E.; Sabeti, P. C.; Myhrvold, C. *Nat. Commun.* **2020**, *11*, 5921.

(17) Feng, W.; Newbigging, A. M.; Tao, J.; Cao, Y.; Peng, H.; Le, C.; Wu, J.; Pang, B.; Li, J.; Tyrrell, D. L.; Zhang, H.; Le, X. C. *Chem. Sci.* **2021**, *12*, 4683−4698.

(18) Hwang, C.; Park, N.; Kim, E. S.; Kim, M.; Kim, S. D.; Park, S.; Kim, N. Y.; Kim, J. H. *Biosens. Bioelectron.* **2021**, *185*, 113177.

(19) Sargsyan, K.; Lin, C.-C.; Chen, T.; Grauffel, C.; Chen, Y.-P.; Yang, W.-Z.; Yuan, H. S.; Lim, C. *Chem. Sci.* **2020**, *11*, 9904−9909.

(20) Vidal-Folch, N.; Gavrilov, D.; Raymond, K.; Rinaldo, P.; Tortorelli, S.; Matern, D.; Oglesbee, D. *Clin. Chem.* **2018**, *64*, 1753−1761.

(21) Jacky, L.; Yurk, D.; Alvarado, J.; Belitz, P.; Fathe, K.; MacDonald, C.; Fraser, S.; Rajagopal, A. *Anal. Chem.* **2021**, *93*, 4208−4216.

(22) Kudo, E.; Israelow, B.; Vogels, C. B. F.; Lu, P.; Wyllie, A. L.; Tokuyama, M.; Venkataraman, A.; Brackney, D. E.; Ott, I. M.; Petrone, M. E.; Earnest, R.; Lapidus, S.; Muenker, M. C.; Moore, A. J.; Casanovas-Massana, A.; Yale, I. R. T.; Omer, S. B.; Dela Cruz, C. S.; Farhadian, S. F.; Ko, A. I.; Grubaugh, N. D.; Iwasaki, A. *PLoS Biol.* **2020**, *18*, No. e3000867.

(23) Byrnes, S. A.; Gallagher, R.; Steadman, A.; Bennett, C.; Rivera, R.; Ortega, C.; Motley, S. T.; Jain, P.; Weigl, B. H.; Connelly, J. T. *Anal. Chem.* **2021**, *93*, 4160−4165.

(24) Alygizakis, N.; Markou, A. N.; Rousis, N. I.; Galani, A.; Avgeris, M.; Adamopoulos, P. G.; Scorilas, A.; Lianidou, E. S.; Paraskevis, D.; Tsiodras, S.; Tsakris, A.; Dimopoulos, M.-A.; Thomaidis, N. S. *Trends Anal. Chem.* **2021**, *134*, 116125.

(25) Mou, X.-B.; Ali, Z.; Li, B.; Li, T.-T.; Yi, H.; Dong, H.-M.; He, N.-Y.; Deng, Y.; Zeng, X. *Chin. Chem. Lett.* **2016**, *27*, 1661−1665.

(26) Liu, R.; Wu, P.; Yang, L.; Hou, X.; Lv, Y. *Mass Spectrom. Rev.* **2014**, *33*, 373−393.

(27) Lin, X.; Guo, W. J.; Jin, L.; Hu, S. *At. Spectrosc.* **2020**, *41*, 1−10.

(28) Liu, J.; Zheng, L.; Shi, J.; Wei, X.; Li, X.; Chen, M.; Wang, M.; Wang, J.; Feng, W. *At. Spectrosc.* **2021**, *42*, 114−119.

(29) Bendall, S. C.; Nolan, G. P.; Roederer, M.; Chattopadhyay, P. K. *Trends Immunol.* **2012**, *33*, 323−332.

(30) Bodenmiller, B.; Zunder, E. R.; Finck, R.; Chen, T. J.; Savig, E. S.; Bruggner, R. V.; Simonds, E. F.; Bendall, S. C.; Sachs, K.; Krutzik, P. O.; Nolan, G. P. *Nat. Biotechnol.* **2012**, *30*, 858−867.

(31) Winter, D. R.; Ledergor, G.; Amit, I. *Nat. Biotechnol.* **2015**, *33*, 931−932.

(32) Winge, R. K.; Peterson, V. J.; Fassel, V. A. *Appl. Spectrosc.* **1979**, *33*, 206−219.

(33) Liu, X.; Zhang, S.-Q.; Cheng, Z.-H.; Wei, X.; Yang, T.; Yu, Y.-L.; Chen, M.-L.; Wang, J.-H. *Anal. Chem.* **2018**, *90*, 12116−12122.

(34) Yan, X.; Yang, L.; Wang, Q. *Anal. Bioanal. Chem.* **2013**, *405*, 5663−5670.

(35) Liu, Z.; Li, X.; Xiao, G.; Chen, B.; He, M.; Hu, B. *Trends Anal. Chem.* **2017**, *93*, 78−101.

(36) Liang, Y.; Yang, L.; Wang, Q. *Appl. Spectrosc. Rev.* **2015**, *51*, 117−128.

(37) Zhang, X.-W.; Liu, M.-X.; He, M.-Q.; Chen, S.; Yu, Y.-L.; Wang, J.-H. *Anal. Chem.* **2021**, *93*, 6437−6445.

(38) Cohen, L.; Walt, D. R. *Chem. Rev.* **2019**, *119*, 293−321.

(39) Li, Z.; Liu, R.; Lv, Y. *Appl. Spectrosc. Rev.* **2021**, 1−26.

(40) Jet, T.; Gines, G.; Rondelez, Y.; Taly, V. *Chem. Soc. Rev.* **2021**, *50*, 4141−4161.

(41) Han, G.; Zhang, S.; Xing, Z.; Zhang, X. *Angew. Chem., Int. Ed.* **2013**, *52*, 1466−1471.

(42) Sun, G.; Huang, B.; Zhang, Y.; Zhang, Y.; Xing, Z.; Zhang, S.; Zhang, X. *Chem. Commun.* **2017**, *53*, 13075−13078.

(43) Yan, X.; Yang, L.; Wang, Q. *Angew. Chem., Int. Ed. Engl.* **2011**, *50*, 5130−5133.

(44) Kang, Q.; He, M.; Chen, B.; Xiao, G.; Hu, B. *Anal. Chem.* **2021**, *93*, 737−744.

(45) Zhang, S.; Han, G.; Xing, Z.; Zhang, S.; Zhang, X. *Anal. Chem.* **2014**, *86*, 3541−3547.

(46) Li, Z.; Li, H.; Deng, D.; Liu, R.; Lv, Y. *Anal. Chem.* **2020**, *92*, 4807−4813.

(47) Guo, H.; Song, X.; Lei, W.; He, C.; You, W.; Lin, Q.; Zhou, S.; Chen, X.; Chen, Z. *Angew. Chem., Int. Ed. Engl.* **2019**, *58*, 12195−12199.

(48) Zhang, S.; Liu, R.; Xing, Z.; Zhang, S.; Zhang, X. *Chem. Commun.* **2016**, *52*, 14310−14313.

(49) Liu, R.; Zhang, S.; Wei, C.; Xing, Z.; Zhang, S.; Zhang, X. *Acc. Chem. Res.* **2016**, *49*, 775−783.

(50) Huang, W.; Ji, M.; Dong, C.-D.; Gu, X.; Wang, L.-M.; Gong, X. G.; Wang, L.-S. *ACS Nano* **2008**, *2*, 897−904.

(51) Hu, J.; Li, Z.; Zhang, H.; Liu, R.; Lv, Y. *Anal. Chem.* **2020**, *92*, 8523−8529.